Journal of Colloid and Interface Science 700 (2025) 138487

Contents lists available at ScienceDirect

Journal of Colloid And Interface Science

journal homepage: www.elsevier.com/locate/jcis

Liquid film thinning-thickening anomaly in electrolyte solutions

Danlong Li [a,b,d], Rogerio Manica [c], Jingqiao Li [c], Bailin Xiang [b], Hainan Wang [a], Qingxia Liu [a,b,c,*], Haijun Zhang [a,**]

[a] School of Chemical Engineering and Technology, China University of Mining and Technology, 221116 Xuzhou, China
[b] Future Technology School, Shenzhen Technology University, Shenzhen 518118, China
[c] Department of Chemical and Materials Engineering, University of Alberta, Edmonton, Alberta T6G 1H9, Canada
[d] IMDEA Nanociencia, C/Faraday 9, 28049 Madrid, Spain

HIGHLIGHTS

- A transition from film thinning to thickening was observed in electrolyte solutions.
- Ion-induced Marangoni flow was confirmed to compete with the normal drainage outflow.
- Theoretical developments were provided to characterize the position of flow balance.
- Specific ion effect on dynamic film evolution was discussed.

GRAPHICAL ABSTRACT

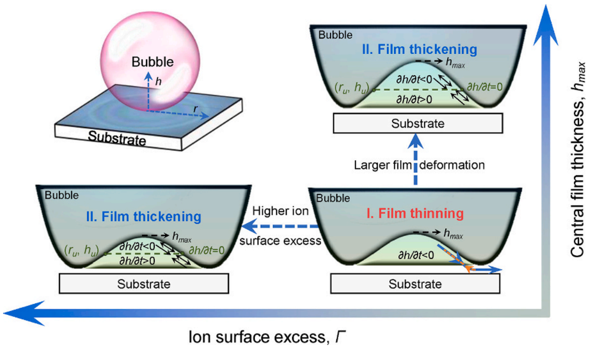

ARTICLE INFO

Keywords:
Bubble
Thin liquid films
Liquid transport
Electrolyte solutions

ABSTRACT

Hypothesis: The distribution of dissolved ions depends largely on the position and shape of air-water interfaces. Following the interfacial interaction, both the surface deformation and reduced separation distance may induce different ion concentrations in liquid film and bulk solutions. The consequent Marangoni effect should change the flow dynamics inside the liquid films and thus influence the film evolution process.
Experiments: In this study, a home-made interferometer is employed to obtain the spatiotemporal evolution of film profiles during the bubble-solid surface interaction. The quantification of film thickness enables the determination of micro/nanoscale fluid flow from liquid films.
Findings: Unlike the common cases of continuous film drainage behaviors, the film thickness at the rim exhibits a counterintuitive increase, causing the previously approaching bubble to retract from solid surfaces. It is revealed how the inward flow can surpass the drainage outflow and reverse the normal film evolution. Theoretical developments involving the electrolyte type, ion concentration and film deformation are provided to describe this competition and address the film thinning-thickening anomaly. Our finding enriches the understanding of the microscopic fluid flow in highly confined and deformed regions, and the research outcome creates the possibility of modulating near-wall bubble dynamics as required.

---

* Corresponding author at: School of Chemical Engineering and Technology, China University of Mining and Technology, 221116 Xuzhou, China.
** Corresponding author.
E-mail addresses: qingxia2@ualberta.ca (Q. Liu), zhjcumt@163.com (H. Zhang).

https://doi.org/10.1016/j.jcis.2025.138487
Received 13 April 2025; Received in revised form 16 July 2025; Accepted 18 July 2025
Available online 20 July 2025

1. Introduction

Water is a precious resource worldwide and all life depends on it. More than 95 % of the water on the earth contains high electrolyte concentrations, which inevitably results in some fascinating phenomena in the natural world and human society with dissolved ions, such as the sea salt aerosols [1], hydrogen production [2] and foaming flow [3]. Owing to the ionic effect on the inhibition of long-range electrostatic forces [4–6], the basic physicochemical processes are more determined by the selective interaction at the microscopic scale, which can be diverse and relate to impressive mechanisms. A typical example concerns the relatively stable bubbles in salty water, which are rarely observed in freshwater (e.g., lakes and rivers) [7]. To describe this phenomenon, previous literature has proposed the ionic distribution principle and the nanoscale solute transport behavior [8,9]. The broad applicability has been substantiated based on the continuous investigation on the ion hydration, molecular orientation within the near-surface region and hydrogen-bonding networks of water in electrolyte solutions [10–12]. Such studies on the ion-water interaction have made significant advances and more recently, experimental evidence has demonstrated that the affinity of ions is region-selective, either enriched in the subsurface area or depleted beyond the outermost surface [13]. This feature clearly suggests that the distribution of ions is strongly influenced by the interfacial geometry and position.

A deformed air-water interface can readily occur during the dynamic interaction of an air bubble with the solid surface in aqueous systems [14–16]. In particular, when ample liquid is present between them, the higher hydrodynamic pressure than the Laplace pressure inside bubbles can induce an inverted air-water interface (called a “dimple”) [17–19]. Accompanying the continuous liquid film drainage, the decreasing distance between the bubble and the solid surface can be presented as a function of space and time [15,20], thereby giving rise to dynamic ion distributions within the near-surface region. The consequent changes in solutal contents inside the intervening liquid should cause surface excess and surface tension gradients along the curved air-water interface, which generates an inward flow to compete with the liquid outflow during film thinning [21]. Depending on the flow competition inside the film region, different thin film dynamics can occur, including thinning, ceasing and thickening behaviors. For example, Velev et al. [22] found the cyclic dimpling phenomenon in emulsion films because of the surfactant redistribution, and Suja et al. [23] reported the evaporation-driven foam stabilization mechanism, which is associated with the solutocapillary Marangoni flows and the consequent fluctuations of film thickness. Herein, by employing the thin-film interference technique, we found that the inverse flow could actively break the flow balance and drive the previously approaching bubble away from the solid surface to some extent, characterized by an increase in the minimum film thickness. This thinning-thickening anomaly prolongs the time required for liquid films to reach the critical thickness (the minimum thickness for liquid films to reach) and reveals a knowledge gap in understanding the counterintuitive microscopic dynamics.

In this work, the whole process of dynamic film evolution is obtained when an air bubble approaches the solid surface in different electrolyte solutions. Analyzing the recorded interference fringes enables the quantification of the film profiles, revealing an unexpected transition from liquid film thinning to thickening. To be specific, the film thickness initially exhibits a rapid reduction due to the decreased range of electrostatic repulsion between the bubble and the solid surface from about 200 nm in Milli-Q water to tens of nanometers in electrolyte solutions. Thereafter, the thinnest position starts to become thicker. Along the highly curved air-water interface, a radial position (r_u) with unchanged thickness (h_u) over time is identified. By reducing the electrolyte concentration or mitigating the deformation at the air-water interface, the r_u position can be transferred to the rim, and the film thickening behavior disappears, suggesting that this phenomenon can be controlled. Based on the established relationship of h_u, the dependence of film evolution on the coupling of electrolyte type, ion concentration and surface deformation is elucidated. The findings are thus expected to provide significant insights for mediating nanoscale fluid flow and controlling bubble behaviors near the solid surface in aqueous systems.

2. Materials and methods

2.1. Materials and solution preparation

Potassium chloride (KCl), sodium chloride (NaCl), and calcium chloride ($CaCl_2$) of ACS grade were bought from Sigma-Aldrich (Merck, Germany). Standard solutions of hydrochloric acid (HCl) and sodium acetate (NaAc) with 1.0 M in concentration were used as received. Before each experiment, the electrolyte powder was calcined at 600 °C for 12 h to remove potential impurities. In each experiment, Milli-Q water with a specific resistivity equal to 18.2 MΩ·cm was employed to prepare the electrolyte solutions. The raw silica wafers were carefully cleaned following the successive stages of pickling and water washing. The dried substrates by a constant nitrogen flow were then placed in a UV-ozone cleaner to ensure the complete removal of surface contaminants. To realize the hydrophobization of wafers for immobilizing air bubbles during the AFM bubble probe measurement, vapor deposition method was employed. The cleaned sample placed on a bracket was initially transferred to a sealed beaker, where 1–2 mL of trimethylchlorosilane (Sigma-Aldrich) was introduced. The silanization reaction occurred through the chemical mechanism of $(CH_3)_3SiCl + -Si-OH \rightarrow HCl + -Si-O-Si(CH_3)_3$, after which the hydrophobized samples were washed rinsed, dried, and collected.

2.2. Thin-film interference technique

High-speed microscopic interferometry is employed to obtain the quantitative data of film evolution between the bubble and the solid substrate. A schematic diagram of the experimental setup is shown in Fig. S1. The bubble motion (approach and retraction) in an observation cell is controlled by a lifting platform, which can be visualized by the side-view high-speed camera (PHOTRON AX50). Once the bubble reaches the solid surface, some liquid will be trapped in between, and light will be reflected off the water-solid and air-water interfaces, respectively. As such, the reflected light can interfere with each other destructively or constructively to form alternately dark and bright rings (called newton rings or interference fringes). As such, the interference fringes can be observed and recorded by the inverted microscope (OLYMPUS IX73) connected with the other high-speed camera (PHOTRON AX200). After the conversion of grayscale images and the extraction of light intensity of interference fringes as a function of time and space $I(r,t)$, the spatiotemporal film thickness $h(r,t)$ can be calculated based on the following expressions. The uncertainty in the estimation of film thickness can be found in Supplementary Materials.

$$h(r,t) = \frac{\lambda}{2\pi n_2}\left(\frac{2m+1}{2}\pi \pm \arcsin\sqrt{\frac{\Delta}{1+4(1-\Delta)\frac{\sqrt{R_{12}R_{23}}}{\left(1-\sqrt{R_{12}R_{23}}\right)^2}}}\right) \tag{1}$$

$$\Delta = \frac{I(r,t) - I_{min}}{I_{max} - I_{min}} \tag{2}$$

$$R_{12} = \frac{(n_1 - n_2)^2}{(n_1 + n_2)^2} \tag{3}$$

$$R_{23} = \frac{(n_2 - n_3)^2}{(n_2 + n_3)^2} \tag{4}$$

where λ represents the monochromatic light wavelength, Δ is the normalized light intensity, I_{min} and I_{max} are the maximum and minimum light intensity, respectively, m denotes the order of interference fringe, n_1, n_2 and n_3 correspond to the reflective indexes of the air bubble, liquid, and silica, respectively [15].

2.3. AFM bubble probe technique

As shown in Fig. S2, the atomic force microscope (AFM, Asylum Research MFP-3D) bubble probe technique can be employed to directly measure the bubble-substrate interaction force during the approach and retraction processes in aqueous systems. Before each experiment, a custom-made tip-less AFM cantilever (rectangular shape: 500 μm × 50 μm × 2 μm) coupled with a circular gold patch (radius 32.5 μm) at the end is initially immersed under the aqueous condition of 10 mM 1-dodecanethiol in ethanol solutions for more than 12 h to complete hydrophobization. In this scenario, the micrometer-sized bubbles previously immobilized on the solid surface with weak hydrophobicity (water contact angle ~30°) can be picked up by the gold patch [4,24,25]. An inverted microscope (Nikon ECLIPSE Ti2) is connected with the AFM system to aid visualizing the prepared cantilever. Subsequently, the AFM bubble probe can be thus transferred to the other hydrophilic solid surface and controlled to interact with target areas of the solid substrate. To make comparison between the experimental and theoretical interaction forces, Eq. (5) can be employed [4].

$$F(t) = 2\pi\int_0^{\infty}[p(r,t) + \Pi(r,t)]rdr \tag{5}$$

where $p(r,t)$ denotes the hydrodynamic pressure, and $\Pi(r,t)$ represents the disjoining pressure. According to the DLVO theory, $\Pi(r,t)$ is mainly contributed by the van der Waals (Π_{vdw}) and electrical double layer interactions (Π_{edl}), which could be calculated as follows [16]:

$$\Pi = -\underbrace{\frac{A}{6\pi h^3}}_{\Pi_{\mathrm{vdw}}} + \underbrace{\left(64nk_BT^*\tanh\left(\frac{ze\phi_s}{4k_BT}\right)^*\tanh\left(\frac{ze\phi_b}{4k_BT}\right)\right)e^{-\kappa h}}_{\Pi_{\mathrm{edl}}} \tag{6}$$

where A denotes the Hamaker constant, h represents the instantaneous film thickness between the bubble and the solid surface, n is the amount of salt ions per unit volume inside the film solution, k_B is the Boltzmann constant, T represents the absolute temperature, ze is the charge of the dissolved ions, ϕ_b and ϕ_s denote the surface potentials of the bubble and the solid surface, respectively, and κ refers to the reciprocal of the Debye length that is correlated with the ion concentration c [26]. Therein, c is considered as 5.6×10^{-6} M in Milli-Q water and ϕ_b is taken as -40 mv [27,28].

2.4. Theoretical models

The fluid flow within the film region is usually described by the Reynolds lubrication theory in Eq. (7) due to the small Reynolds number involved. Additionally, the continuity equation can be expressed in Eq. (8).

$$\frac{\partial p}{\partial r} = \mu\frac{\partial^2 u}{\partial z^2} \tag{7}$$

$$\frac{\partial h}{\partial t} = -\frac{1}{r}\frac{\partial}{\partial r}\left(r\int_0^h udz\right) \tag{8}$$

where $u(r,z,t)$ denotes the fluid velocity inside the liquid film, z is the radial separation distance. Therein, $z = 0$ and $z = h$ correspond to the positions of the solid substrate and the air-water interface. For the interaction of the bubble with the solid surface in pure solvents, combining Eqs. (7) and (8) produces Eq. (9) without the second term on the right-hand side. However, the presence of electrolytes is expected to induce surface tension gradients along the air-water interface, thus giving rise to an additional component following $\mu(\partial u/\partial z) = \partial\sigma/\partial r$ [29]. Consequently, the model for describing the film evolution in electrolyte solutions becomes:

$$\frac{\partial h}{\partial t} = \frac{1}{3\mu r}\frac{\partial}{\partial r}\left(rh^3\frac{\partial p}{\partial r}\right) - \frac{1}{2\mu r}\frac{\partial}{\partial r}\left(rh^2\frac{\partial\sigma}{\partial r}\right) \tag{9}$$

The hydrodynamic pressure $p(r,t)$ can be determined by the Young-Laplace equation in Eq. (10).

$$p = \frac{2\sigma}{R_b} - \frac{\sigma}{r}\left[\frac{\partial h(r,t)}{\partial r} + r\frac{\partial^2 h(r,t)}{\partial r^2}\right] - \Pi \tag{10}$$

3. Results

3.1. Spontaneously thickened liquid film in electrolyte solutions

According to the previous literature [22–24], dissolved ions in solutions can either contribute to or slow down liquid film thinning between the bubble and the solid surface because of the inhibited electrical double-layer interaction and the Marangoni effect. Despite the above effects, the net liquid transport from film regions is generally reported to follow a fixed direction targeting overall drainage [30]. However, as shown in Fig. S3A, the anomalous change of interference fringes in chronological order under the condition of 100 mM KCl is presented. This shows that unlike the normal evolution of alternately dark and bright rings, corresponding the light intensity changing between 0 and 1, the presence of electrolytes can cause partially bright interference fringes at the rim to be darker rather than become completely bright, evidenced by the transition of light intensity from t_1 to t_3 in Fig. S3B. According to the obtained film thickness as a function of time, it can be found that the liquid film starts to become thickened after the film thickness at the rim reaches about 30 nm at t_3 in Fig. S3C. As such, a reversed liquid film evolution can be illustrated in Fig. S3D.

By contrast, Fig. 1A shows a monotonic drainage process in the absence of electrolytes. The liquid film at the rim initially thins faster as it is the thinnest region. Subsequently, the central film thickness exhibits an obvious reduction from 772 nm at 1.44 s to about 120 nm at 18.98 s. During the same period, the rim thickness is only decreased by approximately 50 nm. As such, the dominant position of liquid film drainage is gradually changed from the rim to center until a completely flat liquid film is formed. This outcome can be attributed to the electrostatic repulsion between the negatively charged bubble and silica surfaces, which agrees with the results in previous literature [31]. Under the action of electrolytes, the range of electrostatic forces can be significantly decreased to tens of nanometers. As such, a faster film thinning rate at the rim is observed due to the lack of repulsion (Fig. 1B), evidenced by the rim thickness of 173.9 nm in Milli-Q water and 102.4 nm in 100 mM KCl solution at the same time. Generally, the rim position is the only gateway for liquid exchange between the film the bulk solutions. With decreasing rim thickness, the film thinning rate at the center is expected to slow down, which is responsible for longer duration of the highly curved air-water interface in electrolyte solutions (Fig. 1C and D). As shown in Fig. 2A, it can be found that the liquid film in 100 mM KCl initially keeps drainage until the rim thickness reaches about 39 nm at $t = 8.42$ s. Following this, the central and rim regions show respective decreasing and increasing trends, indicating that the liquid film cannot reach the critical thickness in 100 mM KCl solution before the occurrence of film thickening.

To verify that the van der Waals and electrostatic interactions are consistent with the DLVO theory, the direct force measurement is achieved by employing the AFM bubble probe technique, when the bubble interacts with the solid surface. As shown in Fig. 2B, good consistency between the measurements and theoretical interaction forces in 100 mM KCl solution proves that the prediction by the DLVO theory is accurate. In this scenario, the DLVO forces are not the driver causing the film thickening anomaly. Otherwise, some deviation should occur in Fig. 2B.

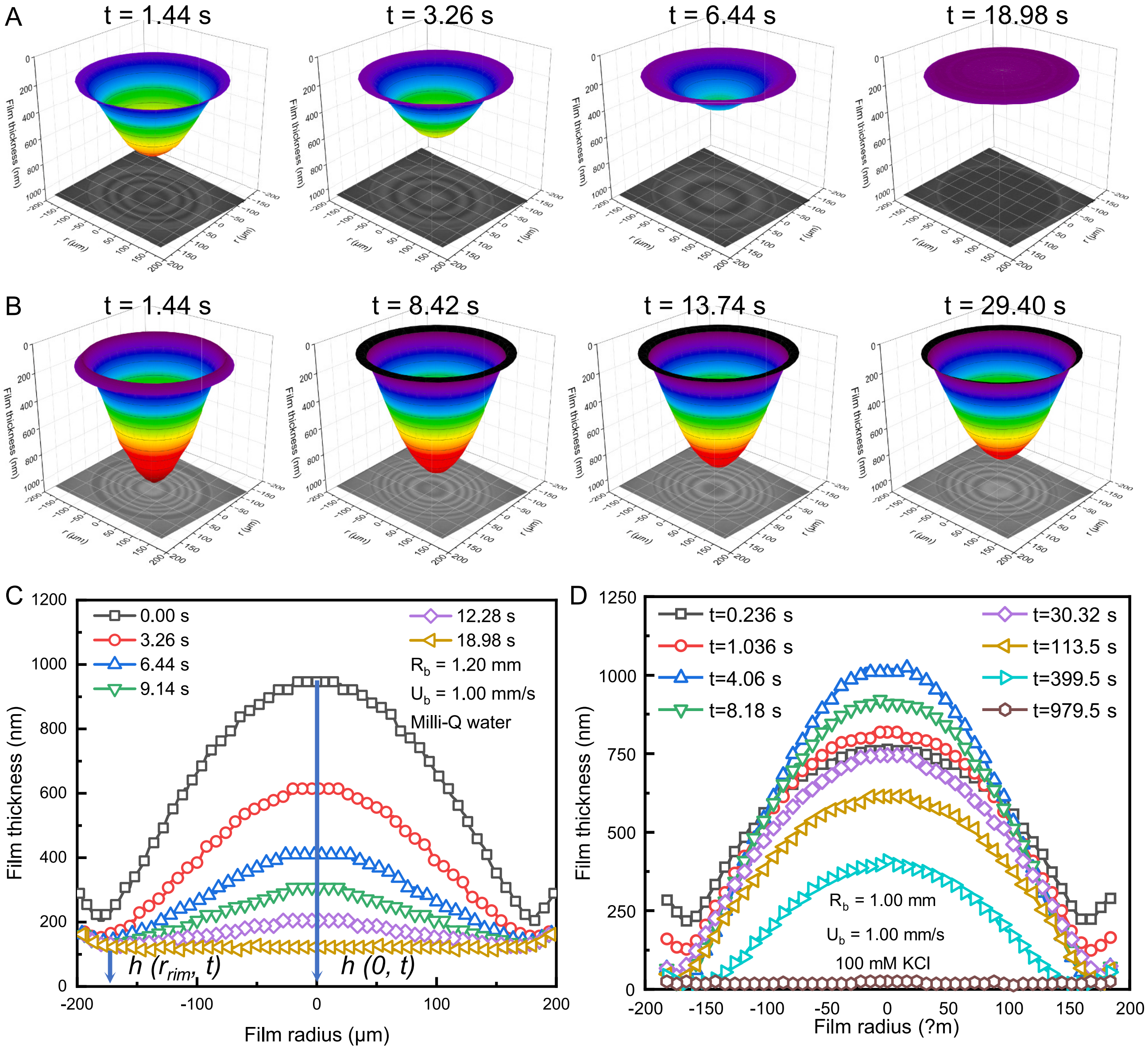

Fig. 1. Three-dimensional film profiles varying with time in (A) Milli-Q water and (B) 100 mM KCl solution ($R_b = 1.20$ mm, $U_b = 1.00$ mm/s). Lifetime of liquid films in (C) Milli-Q water and (D) 100 mM KCl solution.

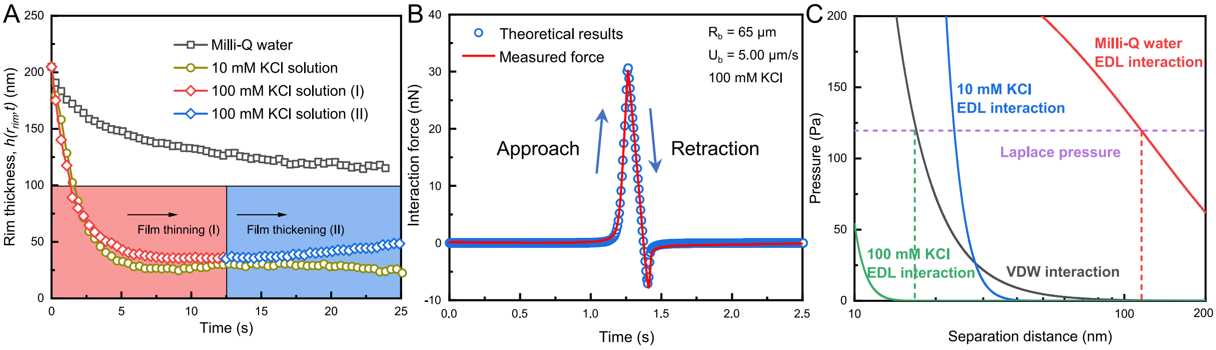

Fig. 2. (A) Evolution of the rim thickness under various aqueous systems ($R_b = 1.00$ mm, $U_b = 1.00$ mm/s). (B) Measured and theoretical interaction forces as a function of time in 100 mM KCl solution. (C) Competition between the Laplace pressure and the disjoining pressure in different solution environment. Therein, the disjoining pressure originates from the van der Waals interaction and electrostatic interaction.

Meanwhile, by further analyzing the time-dependent film evolution process in KCl solutions with respective concentrations of 0 mM (Milli-Q water) and 10 mM KCl, the rim thickness keeps almost unchanged after the equilibrium thickness is reached. Based on the report in previous literature [25,32–34], ϕ_s is equal to -148 mv, -50 mv and -32 mv in 0 mM (Milli-Q water), 10 mM and 100 mM KCl solutions, respectively. With increasing ion concentrations, the Debye length κ^{-1} should be decreased [26], hence limiting the dominant range of electrostatic repulsion. A typical result in electrolyte solutions of different concentrations is displayed in Fig. 2C. Obviously, according to the DLVO theory, the liquid film reaches equilibrium in Milli-Q water due to the electrostatic repulsion between the negatively charged bubble and silica surfaces. By contrast, in 10 mM KCl solution, based on the reduced dominant range of electrical double-layer interaction, the film thickness exhibits until the critical thickness is reached at about $t = 12$ s. Subsequently, the minimum film thickness remains almost unchanged.

It is important to note that the critical film thickness predicted by the DLVO theory is decreased from more than 100 nm in Milli-Q water to about 18 nm in 100 mM KCl solution (Fig. 2C). After the end of film thickening, the liquid film in 100 mM KCl solution finally becomes flattened at about 1000 s (Fig. 1D) and reach the steady state with a thickness of ~18 nm, further validating the accuracy of the DLVO theory. Regarding the transition from normal film drainage in 10 mM KCl solution to film thickening in 100 mM KCl solution, the spontaneously thickened liquid film should largely depend on electrolyte concentrations, which deserves further consideration and investigation.

3.2. *Effect of electrolyte concentrations on film thickening*

To elucidate the underlying mechanism of thickened liquid film, the spatiotemporal evolution of film profiles is analyzed in KCl solutions of higher concentrations. It can be observed from Fig. 3A that at the beginning, the film evolution process exhibits little difference under different conditions. Nevertheless, this situation changes over time when the film thickness reaches a local minimum value h_{min}. Thereafter, the rim thickness is increased by tens of nanometers, as opposed to the decrease of central thickness by hundreds of nanometers (Fig. 3B). With the electrolyte concentrations increasing, the film thickening behavior is identified at a larger rim thickness (Fig. 3A). For example, the rim thickness is increased to about 40 nm in 100 mM KCl solution, compared to more than 70 nm in 300 mM and 600 mM KCl solutions. Additionally, it should be noted that previous literature has found a negligible change of solution viscosity despite the increased KCl concentrations [35,36]. This can also be supported by Figs. 2A, 3A and B where the evolution of film thickness in KCl solutions of different concentrations is almost consistent with each other before the liquid film thinning-thickening anomaly occurs. As such, the effect of solution viscosity on this thickening anomaly can be ruled out.

As shown in Fig. 3C, the rim thickness measured relative to h_{min}, $[h(r_{rim}, t) - h_{min}]$ is limited within the range of approximately 10 nm in 100 mM KCl solution, compared to 40 nm in 300 mM KCl solution and 50 nm in 600 mM KCl solution. Theoretically, larger rim thickness is expected to promote the film thinning behavior at the center. This is attributed to the immobile boundary conditions at the liquid-solid interface where the fluid flow velocity within the near-wall region should exhibit a gradual reduction. [37,38] and thus induce slower liquid outflow rate, which is consistent with faster central film thinning rate in Milli-Q water than in 100 mM KCl solution (Fig. 1A and B). However, on the contrary, regarding larger rim thickness under the condition of high-concentration electrolytes, the central film thinning rate shows an obvious slowdown, and less reduction in the maximum film thickness is measured. For example, the central thickness measured relative to h_{max}, $[h(0, t) - h_{max}]$, is close to 360 nm in 100 mM KCl solution, which is about twice as large as those in the presence of higher concentrations. Such a sharp contrast proves that the influence of ions on liquid film evolution can be region-dependent.

3.3. *Transition between film thinning and thickening*

Based on the analysis of film profiles in Fig. 3C, we can discover an intersection point of different curves, which corresponds to a film thickness (h_u) that does not change over time at the position r_u. For the film thickness larger or smaller than h_u, the respective decreasing or increasing trend can be observed in corresponding film profiles. The comparative evolution of recorded interference fringes shows the dividing line (r_u, h_u). This position can be transferred to the rim without the occurrence of film thickening behavior by employing smaller bubbles (Fig. 4A), suggesting that there exists a bubble size threshold associated with the film thickening behavior. As shown in Fig. 4B, the film thickness at the rim normalized by the bubble radius ($h(r_{rim}, t)/R_b$) can be described as a function of the time nondimensionalized by the viscous time scale ($t/t_c = \sigma t/\mu R_b$) [39]. According to the results, when the bubbles of different size approach the solid surface at the speed of 1 mm/s in 100 mM KCl solution, good consistency can be obtained for

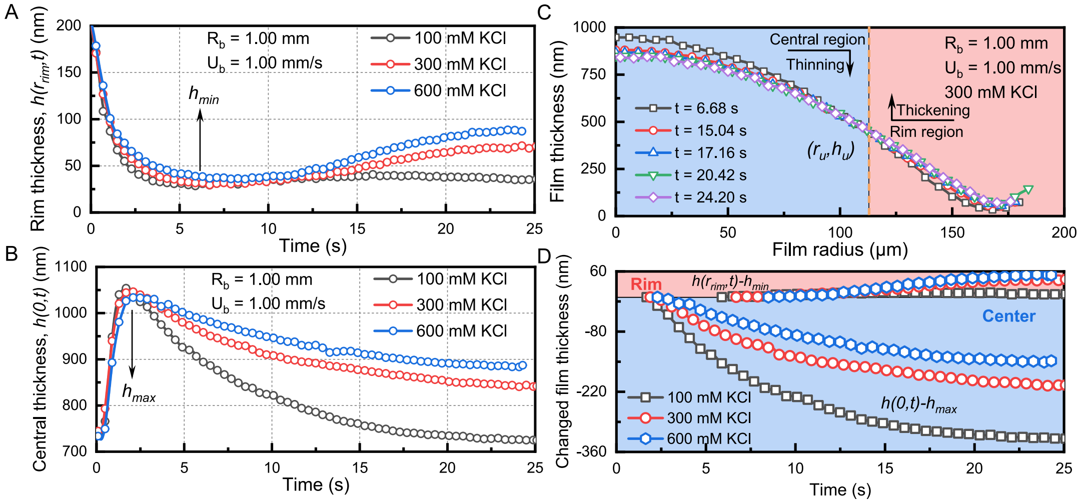

Fig. 3. Time-dependent film thickness at the (A) center $h(0, t)$ and (B) rim $h(r_{rim}, t)$ when the bubble ($R_b = 1.00$ mm, $U_b = 1.00$ mm/s) approaches the substrate. Therein, the local minimum film thickness h_{min} and the local maximum film thickness h_{max} can be obtained when the liquid film transitions from thinning to thickening or from thickening to thinning. (C) Measured film thickness at the rim and the center relative to the local minimum film thickness h_{min} and the local maximum film thickness h_{max}, respectively. (D) Evolution of film profiles in 300 mM KCl solutions.

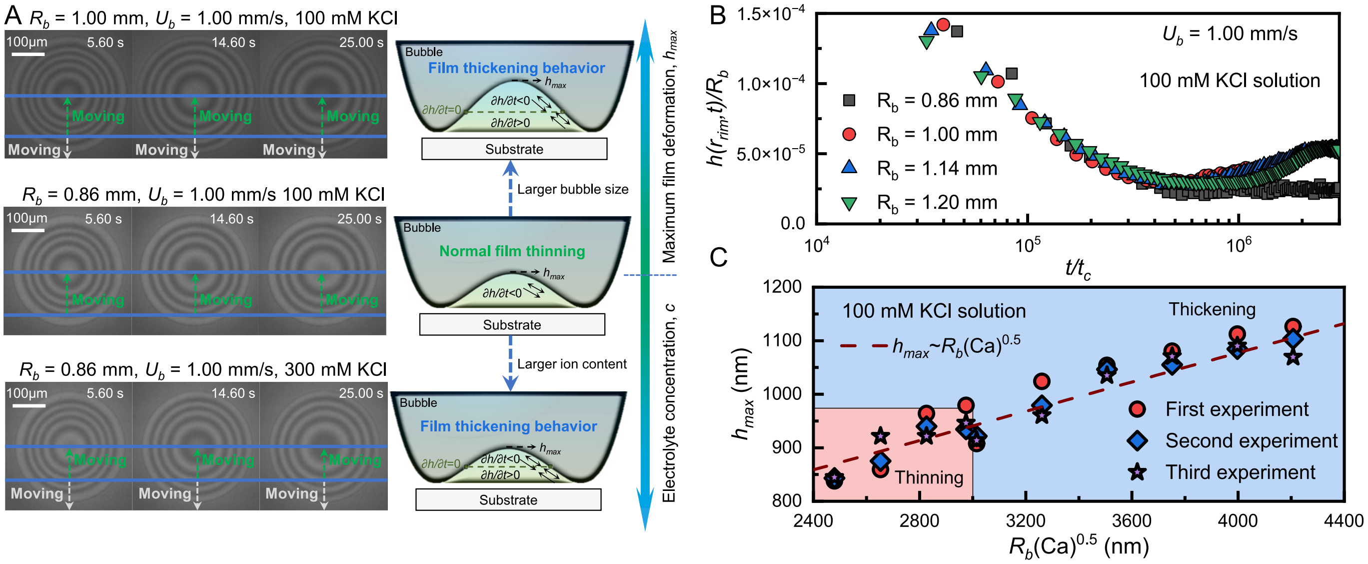

Fig. 4. (A) Illustration of recorded interference fringes describing the influence of maximum film deformation h_{max} and electrolyte concentration c on inducing the film thickening behavior under different conditions. (B) Rim thickness scaled by the bubble radius presented as a function of time nondimensionalized by the viscous time scale. (C) Maximum film thickness h_{max} as a function of $R_b\sqrt{\mathrm{Ca}}$ in 100 mM KCl solution. The results are obtained by employing different bubble velocity (U_b=0.50 mm/s, and 1.00 mm/s) and size (R_b=0.86 mm, 0.93 mm, 1.00 mm, 1.07 mm, 1.13 mm and 1.20 mm).

relatively larger bubbles exhibiting the film thickening behavior. This outcome creates the possibility of characterizing the film thinning-thickening anomaly based on the above relationship. By comparison, for the bubble with 0.86 mm in radius, the liquid film basically remains unchanged after reaching the equilibrium thickness, which is responsible for a deviation from the trend for the other bubble sizes at later times. This outcome suggests that the relationship between $h(r_{rim},t)/R_b$ and t/t_c is applicable to the characterization of both film thinning and thickening behaviors. Regarding the conditions of different U_b, the dimensionless capillary number Ca can be introduced with the rim thickness scaled by $R_b\mathrm{Ca}^{0.25}$ (Fig. S6).

Besides the bubble size, the film thickening behavior can also be observed with increasing electrolyte concentrations. When the KCl concentration is increased to 300 mM, the film thickening behavior is maintained despite small deformation of liquid films (Fig. 4A). As such, in the current study, it is indicated that the threshold of film deformation mainly exists in electrolyte solutions of relatively low concentrations. Basically, the main difference induced by bubble size is associated with the degree of film deformation (dimple height), which can be characterized by h_{max}. For instance, when the bubble radii are equal to 0.86 and 1.00 mm, the central film thickness equals about 800 nm and 1000 nm at 5.60 s, respectively. This is attributed to larger bubbles with lower Laplace pressures, resulting in their weakened ability to resist hydrodynamic pressure. Meanwhile, under the condition of larger bubble motion velocities, the film thickening behavior can be recorded even for small bubbles, which is also associated with the film deformation. Based on the coupling of bubble size and motion velocity, different film deformation can be produced in 100 mM KCl solution.

To provide the theoretical development and predict the change of film deformation, we can start with the Stokes-Reynolds-Young-Laplace equation. At the center of liquid films, the boundary conditions ($\partial p/\partial r = \partial\sigma/\partial r = \partial h/\partial r = 0$) can be applied because of the axisymmetric feature. In this scenario, Eq. (9) can be rearranged into $\partial h/\partial t = \left(h^3/3\mu\right)\left(\partial^2 p/\partial r^2\right) - \left(h^2/2\mu\right)\left(\partial^2\sigma/\partial r^2\right)$. Therein, by introducing $p_0 = \sigma/R_b$, the radial dimension $r_0 = \sqrt{Rh_0}$, and $h_0/t_0 = U_b$ [40], we can obtain the expression of $\mathrm{Ca} \sim h_0^2/3R_b^2 - h_0/2R_b$ ($\mathrm{Ca} = \mu U_b/\sigma$ denotes the capillary number). As such, the relationship between h_{max} and Ca can be simplified as $h_{max} \sim R_b\sqrt{\mathrm{Ca}}$. Similar relationship in the form of $h_{max} \sim R_b\sqrt{\mathrm{Ca}}$ has been reported by Zhang et al. [6], and Bai et al. [40]. By presenting h_{max} as a linear function of $R_b\sqrt{\mathrm{Ca}}$, we can obtain the theoretical value to predict the dynamic film evolution in 100 mM KCl solution (Fig. 4C). As shown, when the value of $R_b\sqrt{\mathrm{Ca}}$ is larger than about 3000 nm, the film thickening anomaly can be observed.

3.4. Flow competition inside the liquid films

In general, the change of film profiles is closely associated with the intervening liquid amount between the bubble and the solid surface [41]. By calculating the trapped liquid volume (V_L) based on the spatiotemporal evolution of film thickness, a significant insight can be provided into the liquid transport behavior inside the film region. Due to the existence of (r_u, h_u), the balance between the inward and outward flows should be reached at that position, making it possible to divide V_L into the trapped liquid volume within the central (V_{Lc}) and rim (V_{Lm}) regions, which can be described as follows:

$$V_L = \int_0^{r_m} 2\pi r h(r,t)dr = \underbrace{\int_0^{r_u} 2\pi r h(r,t)dr}_{V_{Lc}} + \underbrace{\int_{r_u}^{r_m} 2\pi r h(r,t)dr}_{V_{Lm}} \tag{11}$$

According to the respective decreasing and increasing trend of V_{Lc} and V_{Lm} in Fig. 5A, we can confirm that there exist two different flow modes (i.e., outflow and inward flow) inside the film region. With increasing electrolyte concentrations, the inward flow is significantly enhanced, whereas the normal drainage outflow at the center is significantly inhibited. To be more specific, the reduced value of V_{Lc} is about 3.86 pL in 100 mM KCl solution, which is about twice as large as those in the presence of higher KCl concentrations. Such a sharp contrast demonstrates that although the film thinning behavior is dominant at the center, the ion-induced inward flow can mediate the normal drainage outflow from the highly trapped region and thus change film evolution. Notably, the curves illustrating the change of trapped liquid volume are expected to reach the steady state after a certain time interval, and even a declined trend can be observed in 100 mM KCl solution. This result indicates that there exists a duration period for the film thickening behavior, after which the normal film drainage behavior should be recovered. To characterize this duration, the time window within which the stationary point (r_u, h_u) remains unchanged is presented in Fig. 5B.

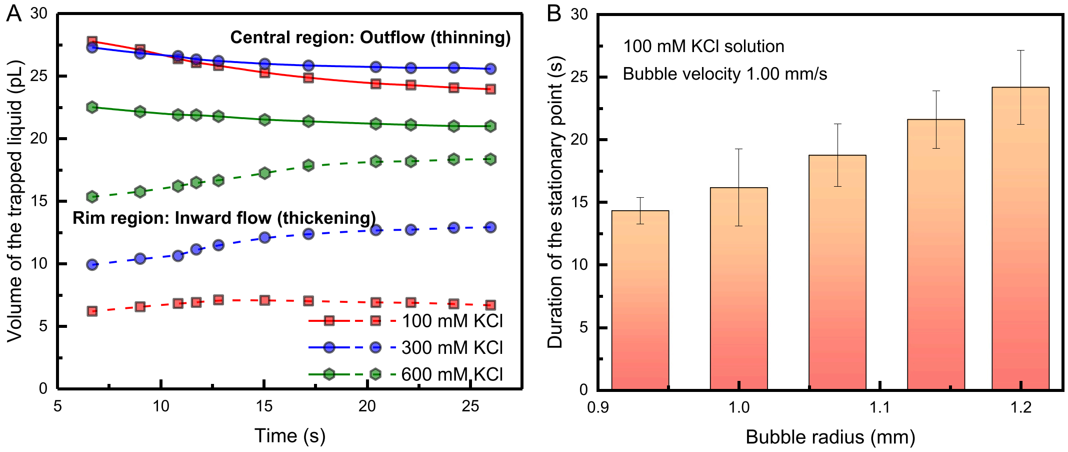

Fig. 5. (A) Changed volume of trapped liquid in the central and rim regions under the condition of different KCl concentrations. (B) Existence time of the stationary point (r_u, h_u) varying with the bubble size in 100 mm KCl solution.

The results show that with the bubble size increasing, the existence time of (r_u, h_u) exhibits an increasing trend. This can be associated with the decreased Laplace pressure of larger bubbles that weakens the ability to promote liquid outflow. In this scenario, the period of flow competition is prolonged.

4. Discussion

4.1. Distance-dependent roles of electrolytes during film evolution

During the interaction between the bubble and the solid surface, dynamic film evolution at large separation distance (> 200 nm) is not substantially influenced by the electrolyte. According to the DLVO theory, the dominant range of the electrical double layer force is around 200 nm in Milli-Q water and less than 20 nm in 100 mM KCl solution, which should be responsible for their consistent film profiles at different times in Fig. 6A. In addition, good consistency between the experimental results and theoretical predictions is obtained by modelling a bubble with mobile interfaces. As such, the purity of employed electrolyte solutions can be guaranteed because even a trace amount of impurities is capable of increasing the hydrodynamic resistance and causing more pronounced deformation at the air-water interface [42,43]. However, as illustrated by Fig. 6B, when the minimum film thickness reaches about 200 nm, the deviation of film thickness in the different aqueous systems occurs. Rapid film thinning behavior can be observed in electrolyte solutions due to the inhibited electrostatic repulsion. Accompanying the continuous bubble-solid surface interaction, a shift from the film drainage mode to the thickening behavior can be observed in Fig. 6C, causing the bubbles to leave the substrate by tens of nanometers. According to the above description, it can be found that role of electrolytes on dynamic film evolution is largely dependent on the separation distance between the bubble and the solid surface, which is presented in Fig. 6 to make a summary.

4.2. Specific ion effect on film thickening

According to the previous literature, it is typical of KCl to be depleted at the air-water interface, which can be characterized by the surface tension increment with concentration ($d\sigma/dc \sim 1.60\ \mathrm{mN{\cdot}m^{-1}{\cdot}M^{-1}}$) [44]. The consequent difference in ion concentrations between the film and bulk solutions can cause surface tension gradients and thus induce an inverse Marangoni flow to compete with the normal drainage outflow [9,45]. Notably, although the decreasing trend of film thickness is dominant at the center, the inverse flow can still slow down the central thinning rate, as evidenced by the decreased liquid outflow at the center with increasing electrolyte concentrations (Fig. 3D). The existence of (r_u, h_u) clearly suggests a balance in flow competition resulting from the normal film drainage and the ion-induced Marangoni effect. To stop film

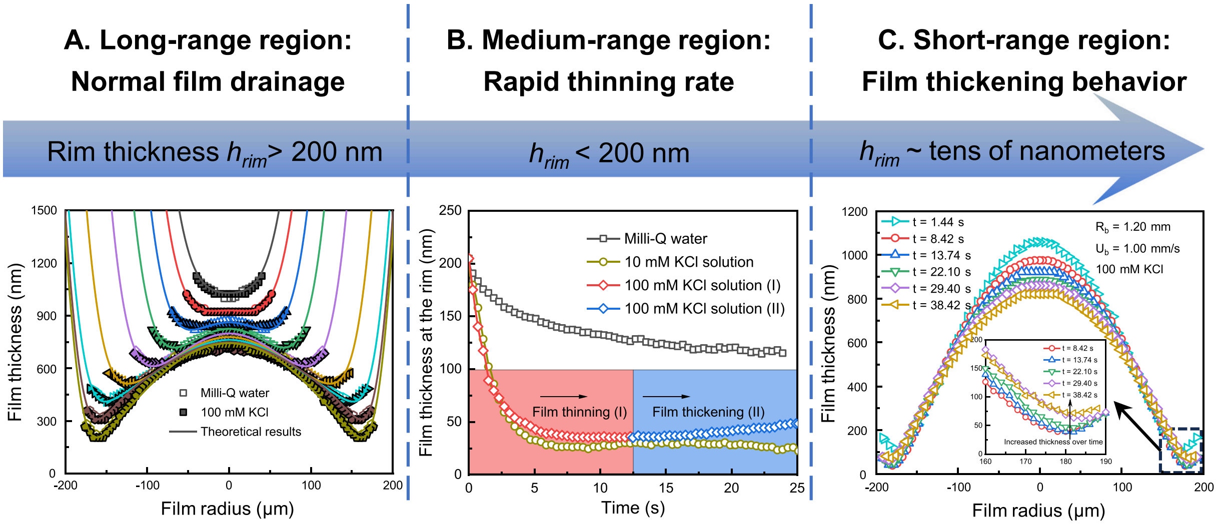

Fig. 6. Illustration for the distance-dependent role of electrolytes during dynamic film evolution between the bubble and the solid surface.

thinning ($\partial h/\partial t = 0$) and maintain the unchanged position (r_u, h_u), the first and second terms in the right-hand of Eq. (9) should be equal, thus giving rise to $\left(h^3/3\mu\right)\left(\partial^2 p/\partial r^2\right) = \left(h^2/2\mu\right)\left(\partial^2 \sigma/\partial r^2\right)$. By applying the scaling analysis, the expression of $\Delta\sigma \sim \sigma h/R_b$ can be obtained. Therein, the surface tension increment $\Delta\sigma$ is equivalent to the product of the changed electrolyte concentration Δc and the surface tension increment with concentration $d\sigma/dc$, namely $\Delta\sigma = \Delta c(d\sigma/dc)$. Considering that the film thickening behavior is dominated by the Marangoni convection [9], the relationship (see Theoretical model of electrolyte transport in supplementary materials) expressed as follows can be employed.

$$\frac{\partial c}{\partial t} \sim -\left(\frac{\partial(rU\Gamma)}{\partial r}\right)\frac{1}{rh} \sim -\frac{V\Gamma}{h^2} = -\left(\frac{\Gamma}{h^2}\right)\left(\frac{dh}{dt}\right) \tag{12}$$

where $\Gamma = -\left(c/R_g T\right)(d\sigma/dc)$ is the ion surface excess (c is the electrolyte concentration, R_g denotes the gas constant, and T is the absolute temperature) [46–48], and $U \sim Vr/h$ denotes the surface velocity during dynamic film evolution [30,49]. Integrating it once yields $\Delta c \sim \Gamma/h$. Therefore, by combining $\Delta\sigma \sim \sigma h/R_b$ and $\Delta\sigma \sim (\Gamma/h)/(d\sigma/dc)$, h_u can be expressed in Eq. (13).

$$h_u \sim \sqrt{\frac{R_g T R_b \Gamma^2}{c\sigma}} \tag{13}$$

It is revealed from the above equation that besides the factors of electrolyte concentration and bubble radius, the ion surface excess Γ can also influence h_u. Because the specific value of Γ is largely dependent on $d\sigma/dc$ that is closely associated with the ion type, experiments are further designed in different electrolyte solutions. For $CaCl_2$ solutions with relatively larger $d\sigma/dc$ (3.60 $mN \cdot m^{-1} \cdot M^{-1}$), a relatively low concentration (100 mM) can induce wider zones for film thickening (Fig. 7A), whereas in 100 mM HCl solution with relatively lower $d\sigma/dc$ (0.28 $mN \cdot m^{-1} \cdot M^{-1}$) [44], most of the film region is dominated by the normal thinning behavior (Fig. 7B).

Along the highly curved air-water interface, the rim regions exhibit more pronounced change of Δc (Fig. 7C). In this scenario, larger surface tension gradients can be produced to cause stronger Marangoni flow to influence the dynamic film evolution, thus accounting for more increase of film thickness in 100 mM $CaCl_2$ solution than in 100 mM HCl solution. Additionally, it can be noticed that the solute concentration gradually builds up over time at the central film region, especially in the presence of 100 mM $CaCl_2$, which is consistent with the slowdown of film

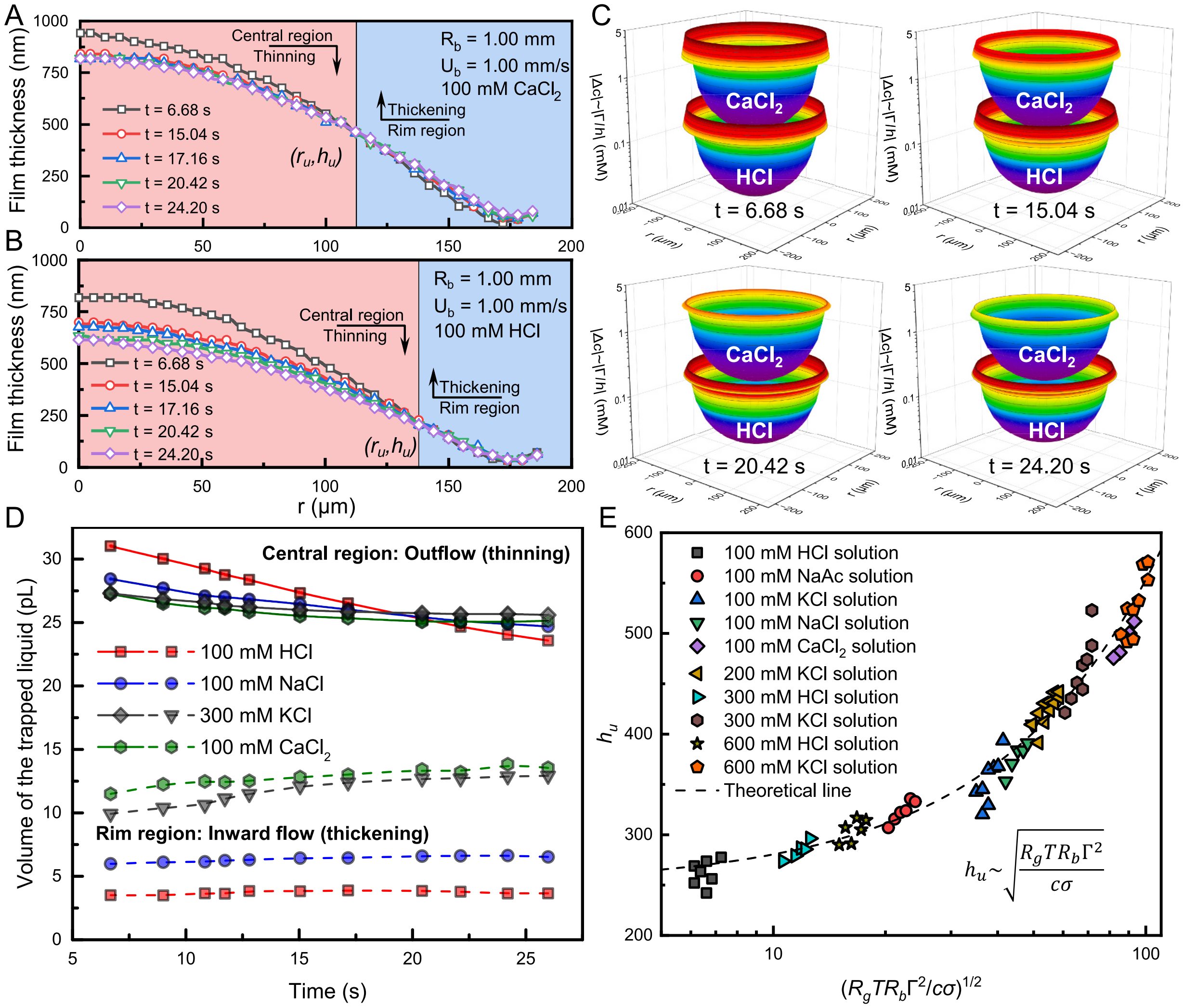

Fig. 7. Comparative film evolution process in (A) 100 mM $CaCl_2$ and (B) 100 mM HCl solutions. (C) Variation in the electrolyte concentration within the liquid film under the condition of 100 mM $CaCl_2$ or HCl solutions. (D) Evolution of the inward flow and outflow from the film regions in different electrolyte solutions. (E) A positive correlation between h_u and $\left(R_g T R_b \Gamma^2/c\sigma\right)^{1/2}$ during film thickening. In 100 mM HCl solution, the liquid film thins faster at the center and the unchanged position (r_u, h_u) is closer to the rim. In contrast, the film thickening anomaly is enhanced in 100 mM $CaCl_2$ solution, evidenced by more inward flow in the rim region in Fig. 7D.

thinning rate at the center. By contrast, due to smaller variation of Δc in 100 mM HCl solution, the consequent inward flow is quite weak and V_{Lm} is only increased by about 0.37 pL, as compared to more than 2.00 pL in 100 mM $CaCl_2$ solution (Fig. 7D). Furthermore, based on Eq. (13), h_u is presented as a function of $\left(R_gTR_b\Gamma^2/c\sigma\right)^{1/2}$, which illustrates a good agreement between the experimental measurements and theoretical predictions. Notably, h_u and r_u have a positive and negative correlation with $\left(R_gTR_b\Gamma^2/c\sigma\right)^{1/2}$, respectively (see Fig. 7E and Fig. S7). This is because with increasing $\left(R_gTR_b\Gamma^2/c\sigma\right)^{1/2}$, inside the liquid film will induce larger ion surface excess Γ to enhance the inverse flow. As such, the unchanged position over time should move towards the central region, thus resulting in the respective increase and decrease of h_u and r_u.

Additionally, the relationship in Fig. 7E indicates that different aqueous systems can exhibit similar liquid transport behaviors. It is obvious that under the condition of unchanged bubble size, the expression of $\left(\Gamma^2/c\right)^{1/2}$ gives rise to comparable results of h_u in 300 mM KCl and 100 mM $CaCl_2$ solutions. This outcome discloses the specific ion effect on dynamic film evolution, and for the electrolytes with larger Γ^2, the inward flow can be enhanced to induce the transition from film thinning to thickening (Fig. 8), demonstrating the dependence of reversible film thickening behavior on the nanoscale flow dynamics.

4.3. Origin of the inverse liquid transport for film thickening

It should be noted that in 100 mM KCl solutions, the total liquid volume ($V_L = V_{Lc} + V_{Lm}$) exhibits a consistent reducing trend, characterized by the decreased liquid volume by about 4 pL after the film thickening anomaly occurs (Fig. 9A). On the one hand, the decrease in V_L indicates that the flow direction points outwards and the outflux at r_m is larger than the corresponding influx. Considering that the rim is the only position for flow exchange between the film and the bulk, there should be no influx from the bulk solution. On the other hand, based on the respective V_{Lc} and V_{Lm} values (Fig. 5A), the inward flow should become dominant at the region near the rim, which is responsible for the film thickening anomaly. The combined results clearly show that in the presence of low electrolyte concentrations, the net influx can only happen from the rim to r_u. This case can correspond to the internal flow recycle despite the uninvolved influx from the bulk solution (Fig. 9B), which demonstrates the existence of surface tension gradients along the air-water interface and the consequent inward flow.

In contrast, with higher electrolyte concentrations (300 mM or 600 mM), the increased V_L value directly proves that the influx at the rim should be larger than the outflux, suggesting that the internal flow circulation and the external flow intervention can jointly influence to the film evolution (Fig. 9C). As such, the inward flow can be contributed by the internal circulation from the rim to r_u, or some additional influx from the bulk to the film region. Especially, with the interventional flow from the bulk, film thinning at the center and film thickening at the rim should be inhibited and promoted, respectively, which agrees well with the results shown in Fig. 3D.

5. Conclusion

The general wisdom has long held that the net flow from the intervening film region follows a fixed direction targeting overall drainage, giving rise to the continuous reduction in film thickness until the equilibrium or instability occurs [4,6,15,20,25,27,31]. Owing to the inhibition effect of electrolytes on relatively long-range electrostatic repulsion between the bubble and the solid surface, the film thickness can reach tens of nanometers where even a small change can make a great influence. For example, previous literature has indicated the existence of Marangoni stresses induced by the concentration gradient in salt solutions, which can cause a flow reversal and prolong the lifetime of liquid films [50,51]. According to the affinity of dissolved ions within the near-surface region, the local ion distributions should vary with the spatiotemporal evolution of air-water interfaces and thus influence the normal film drainage behavior in turn. By inducing the highly curved air-water interface during the bubble-solid surface interaction process, our results reveal a liquid film thinning-thickening anomaly in electrolyte solutions, characterized by the thinnest region exhibiting an increase in the minimum film thickness. Given the principle of mass flow balance [52], the thickened zone of liquid films is clearly associated with an inverse flow surpassing normal drainage outflow. Based on the ion surface excess and consequent surface gradients along the curved air-water interface, the inverse Marangoni-driven flow is introduced to describe its competition with the normal drainage outflow, giving rise to the expression of $h_u \sim \left(R_gTR_b\Gamma^2/c\sigma\right)^{1/2}$, which bridges the dependence of film thickening on the coupling of bubble property and electrolyte type.

The liquid film thinning-thickening anomaly arising from the ion-induced Marangoni flow can be directly associated with the fundamental mechanisms in previous literature. Typical examples involve the different evolution behaviors of hydrogen bubbles on the electrode surface varying with the electrolyte type [53,54], and the prolonged time to reach the critical film thickness during the bubble-solid surface interaction process under higher electrolyte concentrations [30]. Therein, the liquid flow from the film regions can be mediated by the Marangoni effect, thereby inducing the flow competition and change the interphase separation distance. From both the experimental and

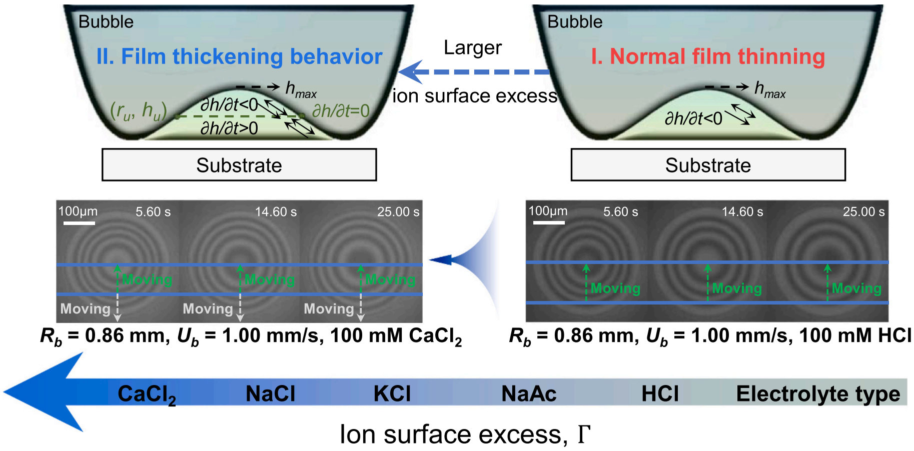

Fig. 8. Schematics illustrating the transition from liquid film thinning to thickening in different electrolyte solutions. A two-way arrow means the simultaneous presence of inward and outward flows. By using two arrows, the flow direction can be characterized by the one-way arrow.

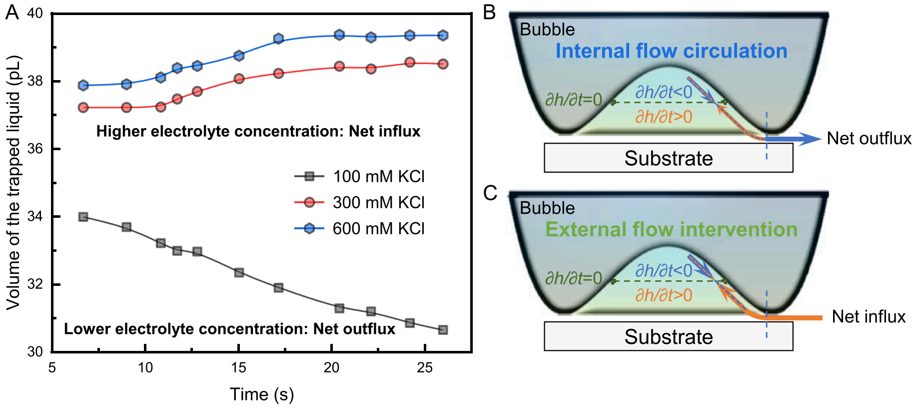

Fig. 9. (A) Evolution of the total liquid volume trapped inside the film region. Illustration of (B) internal flow circulation and (C) external flow intervention responsible for the film thickening anomaly. The dashed line illustrates the existence of inward (orange) and outward (blue) flows, while the solid line represents the dominant flow direction at different regions. (For interpretation of the references to colour in this figure legend, the reader is referred to the web version of this article.)

theoretical perspectives, we address the lack of understanding the liquid film thinning-thickening anomaly, and further enrich the ideas that besides the structural design of solid surfaces and the introduction of external stimuli [55–57], dissolved ions can also influence bubble dynamics by changing the liquid transport, especially in highly confined region. The research outcome is expected to improve the understanding of the role played by the nanoscale fluid flow in the interfacial interaction process and has significant implications for the engineering processes involving bubble attachment/detachment dynamics on the solid surface in saline water, such as seawater flotation and water splitting.

Supplementary data to this article can be found online at https://doi.org/10.1016/j.jcis.2025.138487.

CRediT authorship contribution statement

Danlong Li: Writing – original draft, Investigation, Formal analysis, Data curation, Conceptualization. **Rogerio Manica:** Software, Formal analysis. **Jingqiao Li:** Methodology, Investigation. **Bailin Xiang:** Methodology, Investigation. **Hainan Wang:** Resources, Investigation. **Qingxia Liu:** Writing – review & editing, Visualization, Supervision, Funding acquisition. **Haijun Zhang:** Writing – review & editing, Supervision, Funding acquisition.

Declaration of competing interest

The authors declare that they have no known competing financial interests or personal relationships that could have appeared to influence the work reported in this paper.

Acknowledgments

This work is supported by the National Natural Science Foundation of China (No. 52225405 and No. 52174255) and Pingshan District Innovation Platform Project of Shenzhen Hi-tech Zone Development Special Plan in 2022 (No. 29853M-KCJ-2023-002-02). The authors would also like to appreciate the helpful suggestions from Professor John Ralston.

Data availability

Data will be made available on request.

References

[1] D. Rosenfeld, R. Lahav, A. Khain, M. Pinsky, The role of sea spray in cleansing air pollution over ocean via cloud processes, Science 297 (2002) 1667–1670.
[2] H. Xie, Z. Zhao, T. Liu, Y. Wu, C. Lan, W. Jiang, L. Zhu, Y. Wang, D. Yang, Z. Shao, A membrane-based seawater electrolyser for hydrogen generation, Nature 612 (2022) 673–678.
[3] M. She, T. Weiß, Y. Song, P. Urban, J. Greinert, K. Köser, Marine bubble flow quantification using wide-baseline stereo photogrammetry, ISPRS J. Photogramm. 190 (2022) 322–341.
[4] C. Shi, X. Cui, L. Xie, Q. Liu, D.Y.C. Chan, J.N. Israelachvili, H. Zeng, Measuring forces and spatiotemporal evolution of thin water films between an air bubble and solid surfaces of different hydrophobicity, ACS Nano 9 (2015) 95–104.
[5] L. Xie, J. Wang, Q. Lu, W. Hu, D. Yang, C. Qiao, X. Peng, Q. Peng, T. Wang, W. Sun, Q. Liu, H. Zhang, H. Zeng, Surface interaction mechanisms in mineral flotation: fundamentals, measurements, and perspectives, Adv. Colloid Interface Sci. 295 (2021) 102491.
[6] X. Zhang, R. Manica, P. Tchoukov, Q. Liu, Z. Xu, Effect of approach velocity on thin liquid film drainage between an air bubble and a flat solid surface, J. Phys. Chem. C 121 (2017) 5573–5584.
[7] Y. Katsir, G. Goldstein, A. Marmur, Bubble the wave or waive the bubble: why seawater waves foam and freshwater waves do not? Colloid Interfaces Sci. Commun. 6 (2015) 9.
[8] C.L. Henry, V.S.J. Craig, The link between ion specific bubble coalescence and Hofmeister effects is the partitioning of ions within the interface, Langmuir 26 (2010) 6478–6483.
[9] B. Liu, R. Manica, Q. Liu, Z. Xu, E. Klaseboer, Q. Yang, Nanoscale transport during liquid film thinning inhibits bubble coalescing behavior in electrolyte solutions, Phys. Rev. Lett. 131 (2023) 104003.
[10] Q. Tao, S. Huang, X. Li, X. Chu, X. Lu, D. Wang, Counterion-dictated self-cleaning behavior of polycation coating upon water action: macroscopic dissection of hydration of anions, Angew. Chem. Int. Edit. 59 (2020) 14466–14472.
[11] P. Jungwirth, D.J. Tobias, Specific ion effects at the air/water interface, Chem. Rev. 106 (2006) 1259–1281.
[12] Y. Levin, A.P. Dos Santos, A. Diehl, Ions at the air-water interface: an end to a hundred-year-old mystery? Phys. Rev. Lett. 103 (2009) 257802.
[13] Y. Litman, K. Chiang, T. Seki, Y. Nagata, M. Bonn, Surface stratification determines the interfacial water structure of simple electrolyte solutions, Nat. Chem. 16 (2024) 644–650.
[14] R.F. Tabor, F. Grieser, R.R. Dagastine, D.Y.C. Chan, Measurement and analysis of forces in bubble and droplet systems using AFM, J. Colloid Interface Sci. 371 (2012) 1–14.
[15] D. Li, H. Wang, R. Manica, Z. Zhang, H. Zhang, Q. Liu, Quantifying contributions of different repulsion to film drainage time during the bubble–solid surface attachment and implications for the flotation of fine particles, Langmuir 40 (2024) 10281–10292.
[16] X. Zhang, P. Tchoukov, R. Manica, L. Wang, Q. Liu, Z. Xu, Simultaneous measurement of dynamic force and spatial thin film thickness between deformable and solid surfaces by integrated thin liquid film force apparatus, Soft Matter 12 (2016) 9105–9114.
[17] E. Chatzigiannakis, N. Jaensson, J. Vermant, Thin liquid films: where hydrodynamics, capillarity, surface stresses and intermolecular forces meet, Curr. Opin. Colloid Interface Sci. 53 (2021) 101441.
[18] S. Han, A.V. Nguyen, K. Kim, J. Park, K. You, Quantitative analysis of attachment time of air bubbles to solid surfaces in water, Langmuir 37 (2021) 616–626.
[19] R. Manica, M.H.W. Hendrix, R. Gupta, E. Klaseboer, C. Ohl, D.Y.C. Chan, Effects of hydrodynamic film boundary conditions on bubble–wall impact, Soft Matter 9 (2013) 9755–9758.

[20] M.H.W. Hendrix, R. Manica, E. Klaseboer, D.Y.C. Chan, C. Ohl, Spatiotemporal evolution of thin liquid films during impact of water bubbles on glass on a micrometer to nanometer scale, Phys. Rev. Lett. 108 (2012) 247803.

[21] S.L. Carnie, L. Del Castillo, R.G. Horn, Mobile surface charge can immobilize the air/water Interface, Langmuir 35 (2019) 16043–16052.

[22] O.D. Velev, T.D. Gurkov, R.P. Borwankar, Spontaneous cyclic dimpling in emulsion films due to surfactant mass transfer between the phases, J. Colloids Interfaces Sci. 159 (1993) 497–501.

[23] V. Chandran Suja, A. Kar, W. Cates, S.M. Remmert, P.D. Savage, G.G. Fuller, Evaporation-induced foam stabilization in lubricating oils, Proc. Natl. Acad. Sci. 115 (2018) 7919–7924.

[24] C. Shi, D.Y.C. Chan, Q. Liu, H. Zeng, Probing the hydrophobic interaction between air bubbles and partially hydrophobic surfaces using atomic force microscopy, J. Phys. Chem. C 118 (2014) 25000–25008.

[25] L. Xie, C. Shi, J. Wang, J. Huang, Q. Lu, Q. Liu, H. Zeng, Probing the interaction between air bubble and sphalerite mineral surface using atomic force microscope, Langmuir 31 (2015) 2438–2446.

[26] A.M. Smith, A.A. Lee, S. Perkin, The electrostatic screening length in concentrated electrolytes increases with concentration, J. Phys. Chem. Lett. 7 (2016) 2157–2163.

[27] X. Zhang, R. Manica, Y. Tang, P. Tchoukov, Q. Liu, Z. Xu, Probing boundary conditions at hydrophobic solid–water interfaces by dynamic film drainage measurement, Langmuir 34 (2018) 12025–12035.

[28] D. Hewitt, D. Fornasiero, J. Ralston, L.R. Fisher, Aqueous film drainage at the quartz/water/air interface, J. Chem. Soc. Faraday Trans. 89 (1993) 817–822.

[29] O. Manor, I.U. Vakarelski, X. Tang, S.J.O. Shea, G.W. Stevens, F. Grieser, R. R. Dagastine, D.Y.C. Chan, Hydrodynamic boundary conditions and dynamic forces between bubbles and surfaces, Phys. Rev. Lett. 101 (2008) 024501.

[30] A.C. Palliyalil, A. Mohan, S. Dash, G. Tomar, Ion-specific bubble coalescence dynamics in electrolyte solutions, Langmuir 40 (2024) 1035–1045.

[31] X. Zhang, R. Manica, P. Tchoukov, Q. Liu, Z. Xu, Effect of approach velocity on thin liquid film drainage between an air bubble and a flat solid surface, J. Phys. Chem. C 121 (2017) 5573–5584.

[32] C. Yang, T. Dabros, D. Li, J. Czarnecki, J.H. Masliyah, Measurement of the zeta potential of gas bubbles in aqueous solutions by microelectrophoresis method, J. Colloids Interfaces Sci. 243 (2001) 128–135.

[33] J. Liu, J.D. Miller, X. Yin, V. Gupta, X. Wang, Influence of ionic strength on the surface charge and interaction of layered silicate particles, J. Colloids Interfaces Sci. 432 (2014) 270–277.

[34] M. Kosmulski, Chemical Properties of Material Surfaces, CRC Press, New York, USA, 2001.

[35] M. Firouzi, A.V. Nguyen, Effects of monovalent anions and cations on drainage and lifetime of foam films at different interface approach speeds, Adv. Powder Technol. 25 (2014) 1212–1219.

[36] S. Wang, M. Luo, Y. Sun, C. Wang, X. Song, Experimental data and modeling of viscosity in the quinary system NaCl + KCl + CaCl2 + MgCl2 + H2O, J. Sol. Chem. 53 (2024) 1656–1673.

[37] M. Wegener, N. Paul, M. Kraume, Fluid dynamics and mass transfer at single droplets in liquid/liquid systems, Int. J. Heat Mass Transf. 71 (2014) 475–495.

[38] D.Y.C. Chan, E. Klaseboer, R. Manica, Film drainage and coalescence between deformable drops and bubbles, Soft Matter 7 (2011) 2235–2264.

[39] L. Lombardi, S. Roig-Sanchez, A. Bapat, J.M. Frostad, Nonaqueous foam stabilization mechanisms in the presence of volatile solvents, J. Colloids Interfaces Sci. 648 (2023) 46–55.

[40] T. Bai, R. Manica, B. Liu, E. Klaseboer, Z. Xu, Q. Liu, Water film drainage between a very viscous oil drop and a mica surface, Phys. Rev. Lett. 127 (2021) 124503.

[41] X. Zhang, R. Manica, Q. Liu, Z. Xu, Inward flow of intervening liquid films driven by the Marangoni effect during bubble–solid collisions in ethyl alcohol–NaCl aqueous solutions, Langmuir 37 (2021) 4121–4128.

[42] B. Liu, R. Manica, Q. Liu, E. Klaseboer, Z. Xu, G. Xie, Coalescence of bubbles with mobile interfaces in water, Phys. Rev. Lett. 122 (2019) 194501.

[43] L. Parkinson, J. Ralston, The interaction between a very small rising bubble and a hydrophilic titania surface, J. Phys. Chem. C 114 (2010) 2273–2281.

[44] C.L. Henry, C.N. Dalton, L. Scruton, V.S.J. Craig, Ion-specific coalescence of bubbles in mixed electrolyte solutions, J. Phys. Chem. C 111 (2007) 1015–1023.

[45] L. Parkinson, J. Ralston, Dynamic aspects of small bubble and hydrophilic solid encounters, Adv. Colloids Interfaces 168 (2011) 198–209.

[46] G. Marrucci, L. Nicodemo, Coalescence of gas bubbles in aqueous solutions of inorganic electrolytes, Chem. Eng. Sci. 22 (1967) 1257–1265.

[47] P.K. Weissenborn, R.J. Pugh, Surface tension of aqueous solutions of electrolytes: relationship with ion hydration, oxygen solubility, and bubble coalescence, J. Colloids Interfaces Sci. 184 (1996) 550–563.

[48] D. Li, R. Manica, Z. Chen, S. Wang, Q. Liu, H. Zhang, Bubble coalescence principle in saline water, Proc. Natl. Acad. Sci. U. S. A. 122 (2025) e2417043122.

[49] O. Manor, I.U. Vakarelski, G.W. Stevens, F. Grieser, R.R. Dagastine, D.Y.C. Chan, Dynamic forces between bubbles and surfaces and hydrodynamic boundary conditions, Langmuir 24 (2008) 11533–11543.

[50] V. Chandran Suja, A. Hadidi, A. Kannan, G.G. Fuller, Axisymmetry breaking, chaos, and symmetry recovery in bubble film thickness profiles due to evaporation-induced Marangoni flows, Phys. Fluids 33 (2021) 012112.

[51] E. Sharma, S. Borkar, P. Baumli, X. Shi, J.Y. Wu, D. Myung, G.G. Fuller, Foam stabilization in salt solutions: the role of capillary drainage and Marangoni stresses, J. Colloids Interfaces Sci. 693 (2025) 137535.

[52] E. Klaseboer, J.P. Chevaillier, C. Gourdon, O. Masbernat, Film drainage between colliding drops at constant approach velocity: experiments and modeling, J. Colloids Interfaces Sci. 229 (2000) 274–285.

[53] S. Park, L. Liu, Ç. Demirkır, O. van der Heijden, D. Lohse, D. Krug, M.T.M. Koper, Solutal Marangoni effect determines bubble dynamics during electrocatalytic hydrogen evolution, Nat. Chem. 15 (2023) 1532–1540.

[54] M. Wang, Q. Xu, J. Li, T. Nie, Y. She, L. Guo, Solutal Marangoni effect influencing bubble dynamics with varied electrolyte compositions, Electrochim. Acta 512 (2025) 145448.

[55] S. Zhu, Y. Bian, T. Wu, C. Chen, Y. Jiao, Z. Jiang, Z. Huang, E. Li, J. Li, J. Chu, Y. Hu, D. Wu, L. Jiang, High performance bubble manipulation on ferrofluid-infused laser-ablated microstructured surfaces, Nano Lett. 20 (2020) 5513–5521.

[56] A. Keshmiri, B. Keshavarzi, M. Eftekhari, S. Heitkam, K. Eckert, The impact of an ultrasonic standing wave on the sorption behavior of proteins: investigation of the role of acoustically induced non-spherical bubble oscillations, J. Colloids Interfaces Sci. 660 (2024) 52–65.

[57] M. Hu, F. Wang, L. Chen, P. Huo, Y. Li, X. Gu, K.L. Chong, D. Deng, Near-infrared-laser-navigated dancing bubble within water via a thermally conductive interface, Nat. Commun. 13 (2022) 5749.